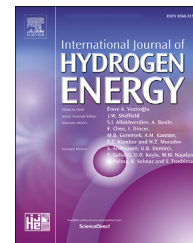




ELSEVIER

Available online at www.sciencedirect.com

ScienceDirect

journal homepage: www.elsevier.com/locate/hydro

Capillaries for water management in polymer electrolyte membrane fuel cells

J.I.S. Cho ^{a,b}, T.P. Neville ^b, P. Trogadas ^{a,b}, J. Bailey ^b, P. Shearing ^b,
D.J.L. Brett ^{b,*}, M.-O. Coppens ^{a,**}

^a EPSRC “Frontier Engineering” Centre for Nature Inspired Engineering & Department of Chemical Engineering, University College London, London WC1E 7JE, United Kingdom

^b Electrochemical Innovation Lab, Department of Chemical Engineering, University College London, London WC1E 7JE, United Kingdom

ARTICLE INFO

Article history:

Received 23 August 2018

Received in revised form

1 October 2018

Accepted 4 October 2018

Available online 29 October 2018

Keywords:

Fuel cell

Water management

Capillary

Laser drilling

Wicking

Flooding

ABSTRACT

Some of the new liquid water management systems in polymer electrolyte membrane (PEM) fuel cells hold great potential in providing flood-free performance and internal humidification. However, current water management systems entail major setbacks, which either inhibit implementation into state-of-the-art architectures, such as stamped metal flow-fields, or restrict their application to certain channel configurations. Here, a novel water management strategy is presented that uses capillary arrays to control liquid water in PEMFCs. These capillaries are laser-drilled into the land of the flow-fields and allow direct removal (wicking) or supply of water (evaporation), depending on the local demand across the electrode. For a 6.25 cm² active area parallel flow-field, a ~92% improvement in maximum power density from capillary integration was demonstrated. The proposed mechanism serves as a simple and effective means of achieving robust and reliable fuel cell operation, without incurring additional parasitic losses due to the high pressure drop associated with conventional serpentine flow-fields.

© 2018 The Authors. Published by Elsevier Ltd on behalf of Hydrogen Energy Publications LLC. This is an open access article under the CC BY license (<http://creativecommons.org/licenses/by/4.0/>).

Introduction

Polymer electrolyte membrane (PEM) fuel cells are a promising alternative source of energy conversion for a wide range of transport, portable, and stationary power applications, due to their high efficiency (>50%), low operating temperature (<100 °C), and high power density [1]. However, water management remains a persistent challenge for PEM fuel cells, especially those using perfluorosulfonic acid (PFSA) type membranes which require effective hydration to ensure good

ionic conductivity [2,3] and longevity [4,5]. If performed properly, humidifying the inlet gases can ensure proper humidification of the membrane, while any excess water that is produced from the electrochemical reaction has to be continuously removed to ensure efficient fuel cell operation. Water droplets accumulating in flow-field channels can cause system instability [6–9], flow maldistribution [10,11], and increase in pressure drop across the flow-field [7,12,13], potentially resulting in long-term performance degradation [9,13–17] and depreciated fuel cell efficiency [13,18,19].

* Corresponding author.

** Corresponding author.

E-mail addresses: d.brett@ucl.ac.uk (D.J.L. Brett), m.coppens@ucl.ac.uk (M.-O. Coppens).

<https://doi.org/10.1016/j.ijhydene.2018.10.030>

0360-3199/© 2018 The Authors. Published by Elsevier Ltd on behalf of Hydrogen Energy Publications LLC. This is an open access article under the CC BY license (<http://creativecommons.org/licenses/by/4.0/>).

Maintaining an adequate water balance in the system is, therefore, imperative for enhanced fuel cell performance, efficiency, and control.

A common strategy to address flooding in PEM fuel cells is via the incorporation of different flow-field designs in the bipolar plates, such as serpentine and interdigitated designs [20–25]. Serpentine flow-fields generate high gas velocity and pressure drop to convectively remove liquid water from the gas channels and the electrode [18,26]. However, the high back-pressure associated with this serpentine design increases the parasitic power losses associated with blowers or compressors [27,28] and lowers the overall fuel cell system efficiency. The gas channels of interdigitated flow-fields are dead-ended, forcing gas to flow through the gas diffusion layer (GDL), thus effectively removing any liquid water that accumulates under the land [29,30]. However, similar to the serpentine configuration, interdigitated geometry also results in high pressure drop across the channel, due to forced convection through the GDL [24,25]. Furthermore, interdigitated flow-fields sustain significant water retention in the channel due to slow gas velocity [30,31]. For these reasons, serpentine remains the preferred configuration for flow-fields in commercial fuel cell systems [32,33].

The simplicity of a parallel flow-field design and the low pressure drop across the channel [27,28] are advantageous for PEM fuel cells. However, the use of parallel geometry is impractical at high humidity operating conditions, since this design leads to excessive flooding when there is a lack of convective gas [6,21,31]. Typically, an air stoichiometry well in excess of 3 is required to prevent parallel channel flooding [34,35].

Despite significant efforts into the development of flow-field channel configurations, such as 3D fine-mesh flow-fields of Toyota Mirai [36–38], a design that accomplishes effective water management at low pressure drop has not yet emerged, primarily due to the closely intertwined nature of these two elements; effective liquid water removal necessitates a high pressure drop to convectively remove liquid water droplets [18]. The inherent difficulty in managing liquid water by using flow-field geometry alone has led to the development of various advanced water management strategies, such as flow-fields with triangular microchannels or microgrooves [39,40]. Wicks mounted [41,42] or directly engineered [43,44] on the channel surface of a flow-field to avoid the formation of liquid slugs have also been tested. Although the implementation of wicking elements improves fuel cell performance thanks to better water management, flooding persists in the mid-current density range, suggesting that the wicks alone do not transport all product water under certain operating regimes, possibly due to an insufficient gas pressure gradient [43,44].

Porous carbon flow-fields with integrated water transport channels for cooling and water removal have also been tested [45–47]. The generated liquid water is directed from the gas channels into internal water transport channels, due to the pressure gradient between the two channels. Under dry operating conditions, the porous carbon flow-fields work in reverse, providing internal humidification as the water in the pores evaporates into the gas channel [35,48]. The main drawback towards commercialization of these flow-fields,

though, is the higher interfacial contact resistance of the porous carbon ($\sim 70 \text{ m}\Omega \text{ cm}^2$ [35]) and the requirement for additional components, namely, a solid graphite frame [35,46] in the fuel cell setup, which increases the overall cost and complexity of the device.

In the present work, a water management strategy for fuel cells is presented based on the incorporation of capillaries in flow-fields. Capillaries are drilled with a laser into the land of a flow-field and hydraulically connected to water transport channels. Liquid water fills the capillaries, and capillary pressure blocks reactant gas entry into the water transport channel. Depending on the local condition of the membrane electrode assembly (MEA), capillaries either remove excess generated water from the electrode via wicking or humidify undersaturated gas streams via evaporation. Contrary to porous carbon plates, capillaries impose negligible additional interfacial contact resistance and can be integrated with a broader range of flow-field designs, including state-of-the-art plates that leverage stamping manufacturing procedures [49–51]. The proposed mechanism is tested on a 6.25 cm^2 active area parallel flow-field, and its performance is evaluated against conventional parallel and double-serpentine flow-fields at fully humidified conditions.

Experimental

Flow-field plate fabrication

The anode and cathode flow-fields were machined from a 1.6 mm thick printed circuit board (PCB) with a $70 \mu\text{m}$ copper layer. PCB-based fuel cells offer the advantage of being low-cost, light-weight, and easily tailored to specific design requirements [8,52–54], which makes the proposed water management strategy highly cost effective in comparison to other previously proposed approaches for water management. A single-serpentine channel was used as the anode flow-field with channel width, spacing and depth of 1 mm. Double-serpentine and parallel flow-fields were used in the cathode with channel width, spacing and depth of 1.2, 1.2, and 0.8 mm, respectively, resulting in channel/active area ratio of 0.54 (double-serpentine) and 0.53 (parallel flow-field).

Water transport channels were embedded in the cathode flow-fields by milling 1.4 mm deep parallel channels on the back-side of these flow-fields in such a way that the resulting land thickness is ca. $200 \mu\text{m}$ (inset of Fig. 1). The ends of the channel were connected by milling 0.5 mm deep perpendicular channels to attain the serpentine configuration.

In the case of parallel flow-fields, bifurcating gas manifolds were introduced at the back-side to ensure uniform gas distribution across the parallel channels on the front-side. Capillaries were laser-drilled into the lands using a Compact Laser Micromachining System (Oxford Lasers, USA). A single laser pulse (0.1 s laser drill time) was sufficient to drill through the $200 \mu\text{m}$ thick copper/FR4 composite layer. A 13×310 capillary array was drilled into each land, which equates to a capillary spacing of $50 \mu\text{m}$. Increasing the capillary number is beneficial in terms of water management, as it increases the total rate of wicking/evaporation. However, the number of capillaries explored in this study was sufficient to mitigate flooding for

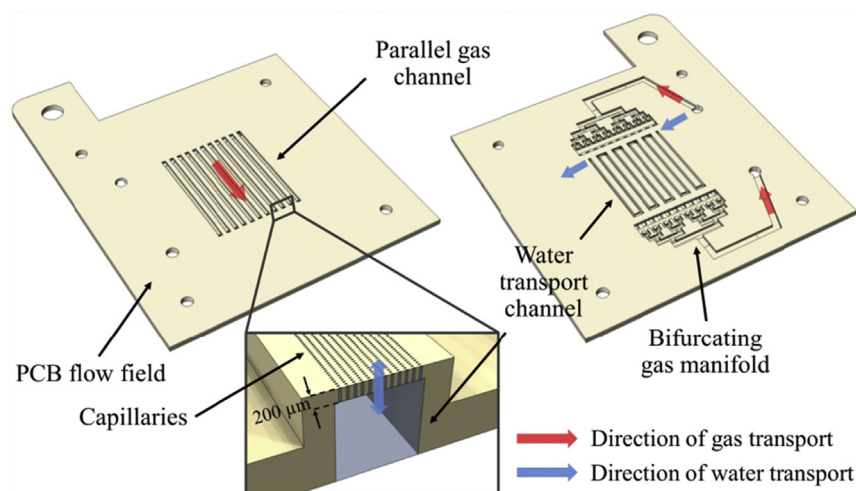


Fig. 1 – Schematic of the parallel flow-field with capillary elements. The front-side (top left) of the plate has parallel gas flow channels and the back-side (top right) features bifurcating gas manifolds and water transport channels. The bifurcating gas manifolds are hydraulically connected to the parallel gas channels and ensure that gas is uniformly distributed across the channels. The inset is a close-up view of the cross-section of the plate with the water transport channel and cylindrical capillaries filled with liquid water. Excess liquid water in the GDL under the land is wicked into the water transport channel through the capillaries, perpendicular to the direction of the gas transport. Where the gas stream is undersaturated, capillaries work in reverse, providing internal humidification as the water in the capillaries evaporates into the GDL.

the investigated fuel cell operating range, as is shown further on (Fig. 5). Also, capillary spacing of less than 50 μm resulted in structural failure of the flow-field land upon cell compression during assembly. Therefore, the 13×310 capillary array was deemed suitable for use in this study. The drilling process took a total of 260 min for 40300 capillaries. A SC4000 abrasive sheet was used to remove burr and melt zones [55,56] created on the surface from the laser drilling.

Ni and Au electroplating

Flow-fields were electroplated in-house in nickel (Balco Engineering, UK) and gold (Spa Plating, UK), prior to laser drilling. The composition of the nickel and gold electroplating solutions were 0.13 M $\text{H}_4\text{N}_2\text{NiO}_6\text{S}_2$ and 0.02 M $\text{KAu}(\text{CN})_2$. A platinum coated stainless steel mesh electrode was used as the counter electrode. The active area region of the flow-field with a 7.5 mm margin around the perimeter was exposed to the electroplating solution (total submerged surface area of 16 cm^2). The copper layer was electroplated in nickel by applying a current of 0.2 A for 3 min. Gold electroplating was accomplished by applying a current of 0.08 A for 94 min to deposit a 5 μm thick gold layer. The current was reduced for gold plating to prevent tarnishing of gold at high potential.

Characterization of capillaries

The laser drilled capillary structure was evaluated using scanning electron microscopy (SEM; Zeiss EVO10, USA) and X-ray tomography (Zeiss Xradia Versa 520, Zeiss, USA). Sample dimensions were 5 mm \times 5 mm \times 200 μm . The sample for SEM measurement was sputter coated with gold for 60 s before imaging, to reduce charging. SEM images were generated at 15 kV. The sample for X-ray tomography was

imaged at 80 kV using a beam power of 7 W with an exposure time of 45 s per radiograph. The optical magnification was $4 \times$ with a pixel size of 2.0 μm . The High Aspect Ratio Tomography (HART) mode was employed to improve the image quality of the flat sample.

The solid bright region in the tomogram (Fig. 2 (b)) corresponds to the metal layer, whereas the bundles of strings and circles in dark grey, indicating a woven fiberglass structure, is the FR4 layer. The epoxy resin that binds the fiberglass is not detected by X-ray tomography, owing to its low attenuation of the beam. Tomogram and SEM images reveal that the capillaries are cylindrical with a slight taper at the top of the copper layer where the laser entered [55–57] and have penetrated all the way through the copper/FR4 composite layer. The capillaries measure $\sim 12.8 \mu\text{m}$ at the entrance diameter and $\sim 6.4 \mu\text{m}$ at the exit diameter, accounting for a total loss of less than 1% in the land area. The capillary pressure generated by the capillaries is 30.2 kPa, which is calculated using [58]:

$$\Delta P_c = \gamma \kappa = \gamma \left(\frac{1}{r_1} + \frac{1}{r_2} \right) \quad (1)$$

where γ (N m^{-1}) is the surface tension of liquid water at 70 $^\circ\text{C}$ and κ (m^{-1}) is the interface curvature, which can be expressed in terms of r_1 (m) and r_2 (m), the principal radii of curvature of the interface. Increasing the capillary diameter may be advantageous in terms of water management, as it increases the rate of wicking and evaporation. However, given the inversely proportional relationship, increasing the capillary diameter leads to a rapid reduction in the capillary pressure, rendering gas breakthrough into the water transport channel more likely. Thus, the capillary diameter of $\sim 12.8 \mu\text{m}$ was used, which was the smallest capillary diameter achievable with the laser system.

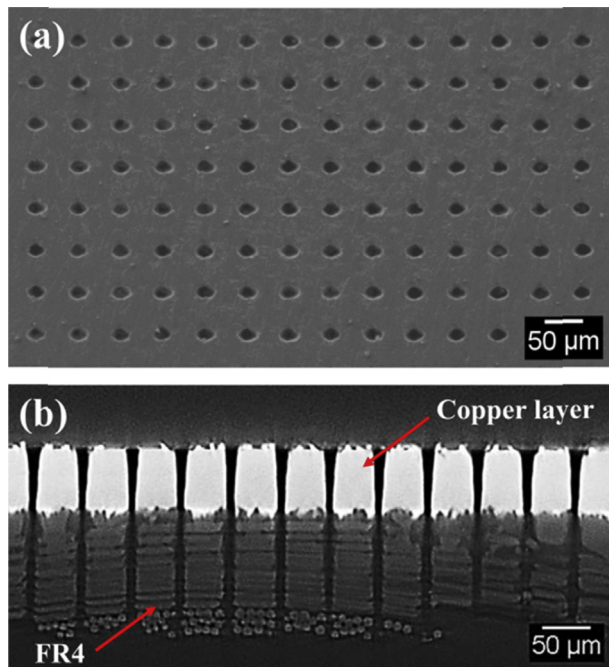


Fig. 2 – (a) SEM image of the capillaries on the copper layer and **(b)** “xz” orthoslice from a tomogram of a cross-section of a PCB layer with a capillary array. The solid bright region of the tomogram corresponds to the copper layer and the dark grey region underneath is the FR4 layer.

Fuel cell assembly

A detailed view of the fuel cell assembly is shown in Fig. 3. It consists of the MEA, anode and cathode flow-fields, gaskets for sealing, a heating plate, an acrylic plate for liquid water transport, and end-plates.

A 6.25 cm² MEA was prepared in-house by hot-pressing a Nafion 212 membrane (DuPont, USA) and ELE0070 gas diffusion electrodes (Johnson Matthey, UK) at 130 °C for 3 min with an applied pressure of 400 psi [59]. The membrane has a thickness of 50 µm and the catalyst layers have a platinum loading of 0.4 mg Pt cm⁻². Tygaflor gaskets (280 µm), placed around each gas diffusion layer (GDL), sealed gases and prevented over-compression.

1/8" PTFE tubing was connected to blind holes ($\phi = 5.5$ mm) on each side of the 12 mm thick acrylic plate using flangeless fittings and ferrules (IDEX, USA). The acrylic plate allowed the water transport channel of the cathode flow-field to be hydraulically connected to a syringe pump (Harvard Apparatus, USA) and a weighing balance (HR-100AZ, A&D, UK), as shown in Fig. 4. The weighing balance could weight a minimum of 0.1 mg and had a recording rate of 10 Hz, which provided sufficient measurement resolution and frequency for accurate quantification of the change in water mass in the water transport channel over a period of 250 s per current density increment of 0.1 A cm⁻². The cell temperature was controlled using a K-type thermocouple (RS pro, UK) and cartridge heaters (RS pro, UK), which were inserted into the stainless steel heating plate. The fuel cell was held together using stainless steel end-plates and was tightened to a torque of

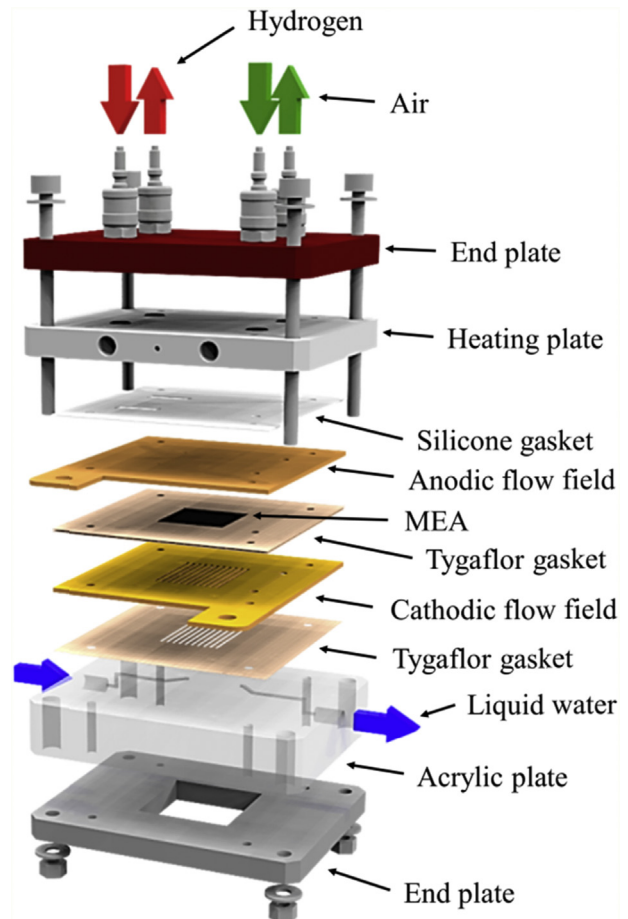


Fig. 3 – Exploded view of the 6.25 cm² fuel cell assembly. The green, red, and blue arrows represent the direction of air, hydrogen, and liquid water, respectively.

1.8 Nm. The assembly was oriented horizontally and reactant gases were fed in co-current orientation during operation.

Test station operation

A schematic of the experimental setup is outlined in Fig. 4. Fuel cell temperature, inlet gas flow rate, relative humidity, and electronic load were regulated using a commercial fuel cell test station (850e, Scribner Associates, USA). The anode (α_{H_2}) and cathode (α_{air}) stoichiometric ratio were maintained at 1.2 and 3, respectively, by controlling the gas flow rate. The fuel cell temperature and relative humidity (RH) of the inlet gas were set to 70 °C and 100%, respectively. During operation, the gas line temperature was kept higher than the humidifier temperature to prevent any condensation prior to entering the fuel cell. Table 1 lists the key experimental parameters used in all experimental measurements.

The fuel cell operating pressure was measured at the gas inlet using a differential pressure transducer (PX139-005D4V, Omega, UK). An in-house computer controlled system (LabVIEW, National Instruments) was used to record data using a data acquisition card (USB 6363, National Instruments).

Polarization curves were obtained by taking data points every 60 s at 0.1 A cm⁻² intervals until either a sudden drop in

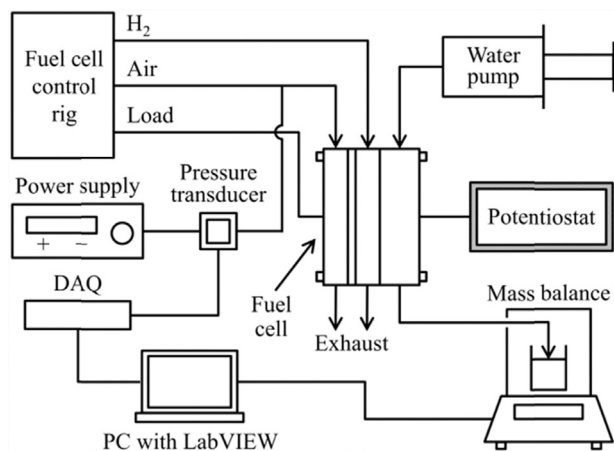


Fig. 4 – Schematic of the experimental setup.

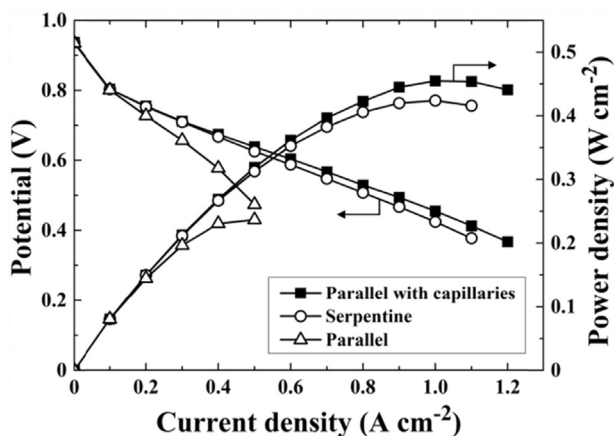


Fig. 5 – Polarization and power density curves obtained for parallel, serpentine, and parallel modified with capillary-containing flow-fields.

fuel cell performance occurred or the potential fell below 0.4 V. Pressure drop was recorded during polarization at a data requisition rate of 5 Hz, and the data were averaged to obtain the mean pressure drop. Transient changes in cell potential were recorded over a period of 250 s at each current density with a data requisition rate of 1 Hz for each current hold experiment.

Table 1 – Experimental parameters used for fuel cell operation.

Parameter	Value
Fuel cell temperature	70 °C
Cathode RH	100%
Anode RH	100%
Hydrogen stoichiometry (α_{H_2})	1.2
Air stoichiometry (α_{air})	3
Number of cathode parallel channels	11
Number of cathode serpentine channels	2
Active area	6.25 cm ²
Membrane	Nafion 212
Electrode	ELE0070
Cathode/anode outlet pressure	1 atm (abs)

Water balance measurements

Changes in the mass of water in the water transport channel were measured at the outlet of the 1/8" PTFE tubing immersed in a 10 ml beaker placed on top of a balance (Fig. 4). Data were recorded over a period of 250 s at each current density with a data requisition rate of 10 Hz. At the start of each experiment, a syringe pump (10 ml min⁻¹ flow rate) was used to fill the PTFE tubing and water transport channel with liquid water. Once capillaries were filled, capillary pressure prevented breakthrough of reactant gas into the water transport channel. Any water that penetrated the gas channel was purged by flowing air at a rate of 0.5 l min⁻¹. Water was not pumped across the water transport channel during the experiment to ensure the reactant gas stream was maintained at a higher pressure than the water transport channel. The pressure difference between the two channels caused excess liquid water in contact with the capillaries to be wicked and transported to the adjacent water transport channel.

Electrochemical impedance spectroscopy (EIS)

EIS was performed using a Gamry Reference 3000 and Gamry Reference 30 K Booster (Gamry Instruments, USA). Prior to the impedance measurement, the fuel cell was conditioned at a constant current to reach steady state. Data points were recorded at a frequency range of 5 kHz to 0.1 Hz (10 frequency points/decade) and AC modulation amplitude was kept below 10% of the DC input signal to ensure a linear system response.

Results and discussion

Polarization curves

Polarization experiments were carried out to evaluate the performance of different cathode flow-fields (Fig. 5). The conventional parallel flow-field experiences inhibited performance, even at a low current density (0.2 A cm⁻²), due to the accumulation of excess liquid water in the electrode and gas channels, as a result of the absence of convective gas flow into the electrode [31,60] and across the channel [27,28]. On the contrary, integration of capillaries in parallel flow-fields dramatically enhances fuel cell performance as liquid water is wicked away from the electrode before it emerges into the channel. Thus, stable and flood-free performance is achieved at all operating points. The parallel flow-field modified with capillaries exhibits a peak power density of 0.46 W cm⁻² at 1 A cm⁻². This represents ~95% and ~7% improvement in peak power density over conventional parallel and serpentine flow-fields obtained at 0.5 A cm⁻² and 1 A cm⁻², respectively.

Galvanostatic testing and electrochemical impedance spectroscopy (EIS) measurements

The above-mentioned improvement in fuel cell performance by the implementation of capillaries in parallel flow-fields was verified by galvanostatic measurements (Fig. 6). Stable fuel cell performance is achieved with the serpentine flow-field. This is attributed to the faster gas flow and higher pressure drop,

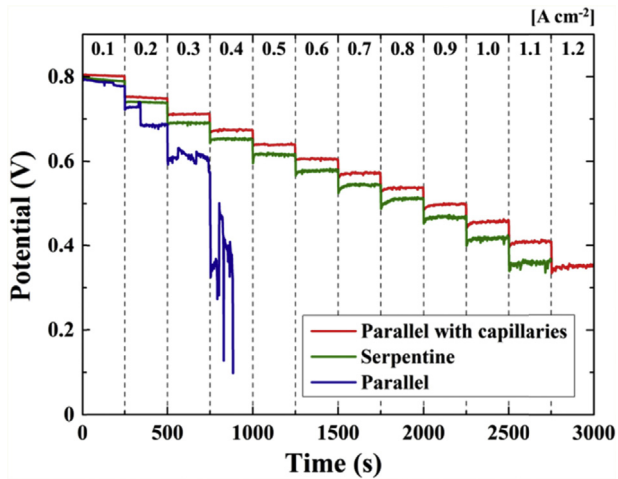


Fig. 6 – Current hold experiment conducted for different flow-fields.

which facilitate convective water removal in the porous media and channel. By comparison, the fuel cell performance of the parallel flow-field is highly unstable, as indicated by erratic potential fluctuations at low current density. Such transient potential yields insight into flooding events [18,61]. A gradual decline in fuel cell performance, followed by abrupt, temporary recovery alludes to liquid water accumulation in the channel or manifold, which intermittently purges, once it exceeds the critical liquid water content [62–64].

The introduction of capillaries greatly improves the transient stability of the parallel flow-field based fuel cell. Stable fuel cell performance indicates that flooding in the gas channel is mitigated throughout the investigated operating region, as the liquid water is removed directly from the electrode before the formation of droplets in the channel. This result suggests that water management using capillaries reduces the dependence of the modified flow-field on convective gas flow for liquid water removal. As a result, the parallel flow-field modified with capillaries shows greater improvement in fuel cell performance over a serpentine flow-field at higher current densities, implying enhanced mass transport, despite the lack of convective gas transport within the electrode.

Electrochemical impedance spectroscopy (EIS) was conducted to elucidate this improvement in performance (Fig. 7).

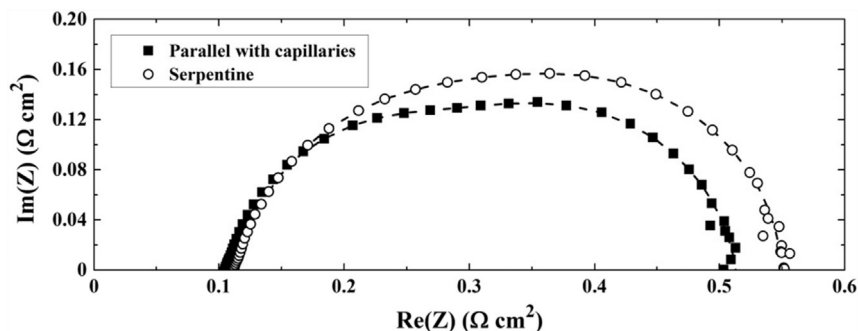


Fig. 7 – Nyquist plots taken at 0.5 A cm^{-2} for different flow-fields. EIS was not conducted on the parallel flow-field, due to excessive fluctuations in data points, as a result of system instability. Dotted lines are fitted results.

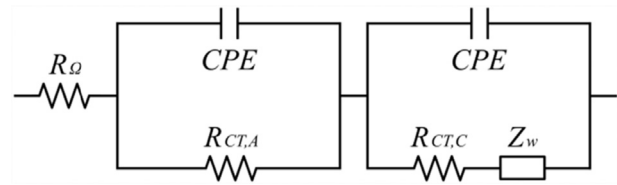


Fig. 8 – Equivalent circuit diagram for impedance analysis. R_{Ω} is the Ohmic resistance, CPE is the constant phase element, Z_w is the Warburg element, and $R_{CT,A}$ and $R_{CT,C}$ are the anodic and cathodic charge transfer resistance, respectively.

The measured impedance spectra were fitted using the Simplex method in Gamry EChem Analyst, based on the equivalent circuit diagram in Fig. 8, to deconvolute the extent of the contribution of each phenomenon to the overall fuel cell performance losses.

The values of the charge transfer (R_{CT}) and mass transport (R_{MT}) resistances for the parallel flow-field modified with capillaries are $0.16 \text{ } \Omega \text{ cm}^2$ and $0.41 \text{ } \Omega \text{ cm}^2$, and for the serpentine flow-field, they are $0.18 \text{ } \Omega \text{ cm}^2$ and $0.44 \text{ } \Omega \text{ cm}^2$, respectively. Thus, the improvement in reaction rate and mass transport is attributed to better liquid water removal in the porous media facilitated by capillaries. Improved liquid water removal increases catalyst utilization and enhances the overall reaction rate, as more active sites are made available. Mass transport within the electrode is also improved from reduced diffusional losses, as fewer pores are blocked with liquid water and catalytic sites are more readily available. Although the serpentine geometry is known to achieve superior water removal, local flooding is anticipated in regions around the channel bends [26,65], which could have contributed to its higher overall system impedance.

High-frequency resistance (HFR)

High-frequency resistance (HFR) measurements were conducted to ensure that membrane hydration and interfacial contact resistance are similar for all flow-fields (Fig. 9). Maintaining adequate membrane hydration is imperative for proper proton conduction and oxygen mass transport [66–68]. The HFR value is highest at 0.1 A cm^{-2} , and it gradually declines as the membrane becomes more hydrated from liquid

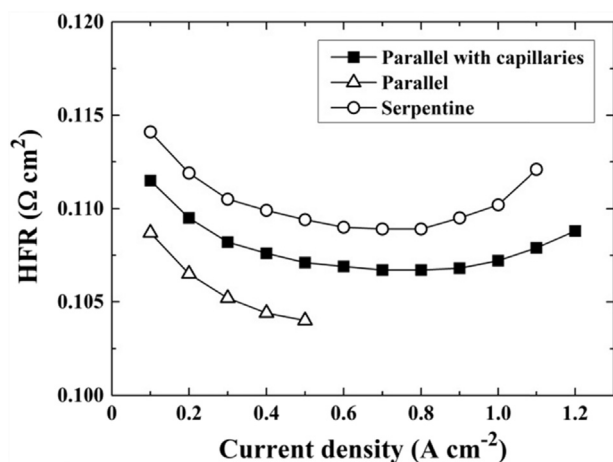


Fig. 9 – Change in high-frequency resistance (HFR) with respect to current density for different flow-fields.

water generation. The membrane starts to dehydrate slightly at high current densities ($>0.9 \text{ A cm}^{-2}$), due to the increased local temperature of the MEA [69–71], fostering water evaporation.

A slight discrepancy in HFR values between parallel and serpentine flow-fields may have stemmed from the difference in channel configuration, such as land/channel ratio and channel spacing. The presence of capillaries in the parallel flow-field leads to a small reduction in the contact area between GDL and land, which slightly increases its interfacial contact resistance. However, such marginal difference in the value of HFR is negligible, as it only accounts for a potential drop of 2.7 mV and 1.6 mV at 0.5 A cm^{-2} for the serpentine and parallel flow-field modified with capillaries, in comparison to the parallel flow-field.

Rate of wicking and evaporation

To investigate the influence of current density on the water balance, the mass change of water in the water transport channel was used as a measure of the rate of wicking or evaporation through the capillaries (Fig. 10). A positive rate of mass change indicates that there is a net excess of water transported from the electrode to the water transport channel (wicking), while a negative value indicates a net excess transport of water from the water transport channel to the cathode flow-field (evaporation).

At low current densities ($\leq 0.5 \text{ A cm}^{-2}$), the generated liquid water is wicked into the water transport channel through capillaries via the pressure differential between gas and water transport channels. The rate of wicking increases with current density, due to the larger amount of water generated at the cathode. Although cathode flooding is typically associated with high current density operation, due to increased water production and electro-osmotic drag from the anode [18], flooding has been shown to occur at a relatively low current density of 0.1 A cm^{-2} due to low gas velocity [72]. Unoptimised water management is one of the main causes of irreversible performance degradation and is an issue across the full range of current density. Here, wicking through capillary channels is

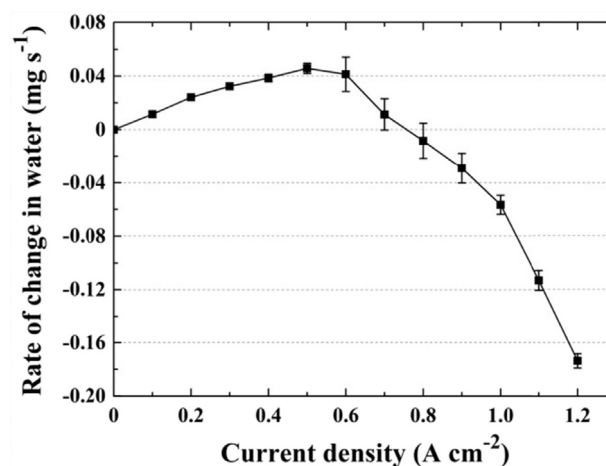


Fig. 10 – The rate of change of water mass in water transport channels with respect to current density for a parallel flow-field modified with capillaries.

shown to be an effective means of mitigating flooding at low current density.

The net rate of water transfer in the wicking direction declines with current density at mid-range values ($0.6 \leq j \leq 0.8 \text{ A cm}^{-2}$). Increased current heats the fuel cell and causes more water to evaporate from the capillaries. This is not a homogeneous effect and will be most pronounced in regions where local saturation pressure is higher, due to heat generated in the catalyst layer [70,71,73,74]. In this operating window, capillaries internally humidify undersaturated gas streams, while removing excess generated water in the electrode. The capillaries remain saturated with liquid water by movement of water from the water transport channel. Since MEA temperature tends to increase towards the gas channel outlet [74,75], a gradual transition in water management mechanism from wicking to evaporation is expected along the flow path [45,73].

Beyond 0.8 A cm^{-2} , evaporation takes over as the dominant form of liquid water transport mechanism for the cell as a whole, due to the rise in cell temperature. This phenomenon agrees with the HFR results, which show membrane dehydration above 0.8 A cm^{-2} . Studies report a typical cell temperature rise of $10 \text{ }^\circ\text{C}$ or more at high current densities, which can lead to significant membrane dehydration [70,71]. A simplified water mass balance calculation in the cathode suggests that a $10 \text{ }^\circ\text{C}$ rise in MEA temperature vastly increases the evaporation rate, satisfying the overall water mass balance without the need for wicking (Fig. S1). This finding is consistent with neutron imaging work that has shown that at high current densities, flooding is partly mitigated by a temperature increase due to internal heating [76]. These results suggest that such a capillary system could be used to deliver internal gas humidification for fuel cells operating on dry inlet gases. Elimination of the gas humidification system potentially simplifies the overall fuel cell system and is beneficial both in terms of maintenance and operating cost. This will be the subject of future work.

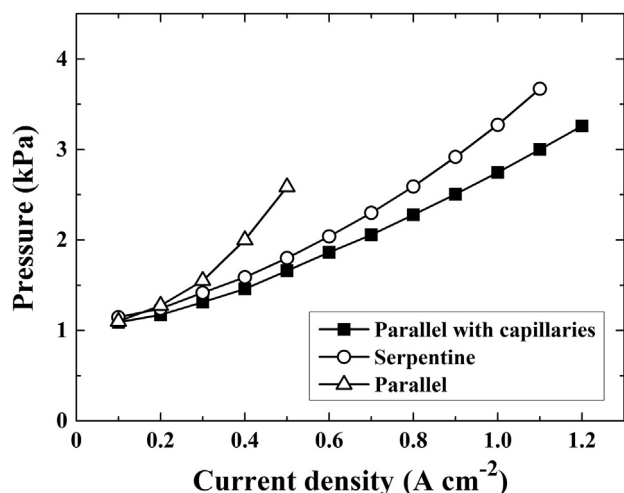


Fig. 11 – Change in pressure drop across the cathode with respect to current density for different flow-fields.

Pressure drop

Finally, in terms of pressure drop (Fig. 11), the unmodified parallel flow-field exhibits the highest value at low current densities (prior to flooding). This observation is in contrast to previous reports displaying significantly higher pressure drop for a serpentine channel than a parallel one, due to faster gas flow and a longer channel path [27,28,31]. We attribute this anomaly to the constriction and blockage of the gas flow path arising from excess liquid water in the gas channels and bifurcating manifolds [27]. A similar pressure drop recorded for the parallel and serpentine flow-fields at 0.1 A cm^{-2} , where flooding is largely mitigated, suggests that the additional hydraulic resistance stemming from the bifurcating manifolds also significantly adds to the pressure drop over the parallel flow-field.

The parallel flow-field modified with capillaries displays the lowest pressure drop, reducing the parasitic energy consumption by air blowers [77,78]. Hence, the inherent advantage of the parallel flow-field is preserved, owing to the unobtrusive design and superior water management of the capillaries. The ability of the parallel flow-field modified with capillaries to manage liquid water and deliver a low-pressure drop is therefore highly desirable from the perspective of operating cost.

Conclusions

An approach to achieve efficient water management in PEM fuel cells using capillaries has been presented. The stability and operating range of a parallel flow-field have been shown to markedly improve with this advanced water management mechanism, as channel flooding is mitigated against by direct liquid removal from the channel. This mechanism combines water removal in areas and impeded conditions liable to flooding with a humidification role in regions where the gas stream has a lower water vapour pressure, due to higher temperature or supply of dry gas. Thus, the capillaries allow

redistribution of liquid water within the cell by removing or supplying water, depending on the local demand across the MEA. This demonstrates the excellent adaptability of the mechanism to different operation conditions. The parallel flow-field modified with capillaries exhibited ~95% and ~7% improvement in peak power density over the conventional parallel and serpentine flow-fields, respectively.

The proceeding work will focus on testing flow-fields modified with capillaries under dry operating conditions to validate the gas humidification capacity of the mechanism. This would allow efficient and robust fuel cell operation across a wide range of operating conditions expected to be confronted by a PEM fuel cell during its lifetime. Further work will concentrate on the scalability of these flow-fields, making local measurements of current, temperature, and water; optimisation of capillary size, density, and location; and effect of cell orientation and the nature of channel wall materials (hydrophobic/hydrophilic). With respect to scalability, the capillary diameter explored in this study may not be sufficiently small to prevent gas breakthrough into the water transport channel for larger fuel cell systems, as gas pressure significantly increases during scale-up. Fabrication of narrower capillaries is therefore desirable, which will be investigated in the following work, possibly with the use of a more advanced laser system (e.g., femtosecond laser). However, the principles are similar to those discussed here.

Conflict of interest disclosure

The authors declare no competing financial interest.

Acknowledgements

The authors gratefully acknowledge financial support from an EPSRC “Frontier Engineering” Award (EP/K038656/1) and a UCL Faculty of Engineering Sciences Dean's Scholarship for Jason I. S. Cho. They also thank the EPSRC Centre for Grid-Scale Energy Storage (EP/L014289/1) for access to X-ray tomography equipment and EPSRC funding to the Electrochemical Innovation Lab for supporting this work (EP/M014371/1, EP/M023508/1, EP/M009394/1 and EP/P009050/1). Paul Shearing acknowledges the Royal Academy of Engineering for a Chair in Emerging Technologies.

Appendix A. Supplementary data

Supplementary data to this article can be found online at <https://doi.org/10.1016/j.ijhydene.2018.10.030>.

REFERENCES

- [1] White RT, et al. 3D printed flow field and fixture for visualization of water distribution in fuel cells by X-ray computed tomography. *J Electrochem Soc* 2016;163(13):F1337–43.

- [2] Matos BR, Santiago EI, Fonseca FC. Irreversibility of proton conductivity of Nafion and Nafion–Titania composites at high relative humidity. *Materials for Renewable and Sustainable Energy* 2015;4(4):16.
- [3] Zawodzinski TA, et al. Water uptake by and transport through Nafion® 117 membranes. *J Electrochem Soc* 1993;140(4):1041–7.
- [4] Sethuraman VA, et al. Durability of perfluorosulfonic acid and hydrocarbon membranes: effect of humidity and temperature. *J Electrochem Soc* 2008;155(2):B119–24.
- [5] Karpenko-Jereb L, et al. Membrane degradation model for 3D CFD analysis of fuel cell performance as a function of time. *Int J Hydrogen Energy* 2016;41(31):13644–56.
- [6] Bachman J, et al. Experimental investigation of the effect of channel length on performance and water accumulation in a PEMFC parallel flow field. *Int J Hydrogen Energy* 2012;37(22):17172–9.
- [7] Liu X, et al. Water flooding and pressure drop characteristics in flow channels of proton exchange membrane fuel cells. *Electrochim Acta* 2007;52(11):3607–14.
- [8] Wu Y, et al. Effect of serpentine flow-field design on the water management of polymer electrolyte fuel cells: an in-operando neutron radiography study. *J Power Sources* 2018;399:254–63.
- [9] Zhang X, et al. Effects of carbon corrosion on mass transfer losses in proton exchange membrane fuel cells. *Int J Hydrogen Energy* 2017;42(7):4699–705.
- [10] Kandlikar SG, et al. Measurement of flow maldistribution in parallel channels and its application to ex-situ and in-situ experiments in PEMFC water management studies. *Int J Heat Mass Tran* 2009;52(7):1741–52.
- [11] Zhang L, et al. Gas flow rate distributions in parallel minichannels for polymer electrolyte membrane fuel cells: experiments and theoretical analysis. *J Power Sources* 2010;195(10):3231–9.
- [12] Barbir F, Gorgun H, Wang X. Relationship between pressure drop and cell resistance as a diagnostic tool for PEM fuel cells. *J Power Sources* 2005;141(1):96–101.
- [13] Trogadas P, et al. A lung-inspired approach to scalable and robust fuel cell design. *Energy Environ Sci* 2018;11(1):136–43.
- [14] Taniguchi A, et al. Analysis of electrocatalyst degradation in PEMFC caused by cell reversal during fuel starvation. *J Power Sources* 2004;130(1):42–9.
- [15] Schmittinger W, Vahidi A. A review of the main parameters influencing long-term performance and durability of PEM fuel cells. *J Power Sources* 2008;180(1):1–14.
- [16] Meyers JP, Darling RM. Model of carbon corrosion in PEM fuel cells. *J Electrochem Soc* 2006;153(8):A1432–42.
- [17] Borup R, et al. Scientific aspects of polymer electrolyte fuel cell durability and degradation. *Chem Rev* 2007;107(10):3904–51.
- [18] Li H, et al. A review of water flooding issues in the proton exchange membrane fuel cell. *J Power Sources* 2008;178(1):103–17.
- [19] Wu H-W. A review of recent development: transport and performance modeling of PEM fuel cells. *Appl Energy* 2016;165:81–106.
- [20] Li X, Sabir I. Review of bipolar plates in PEM fuel cells: flow-field designs. *Int J Hydrogen Energy* 2005;30(4):359–71.
- [21] Su A, et al. Studies on flooding in PEM fuel cell cathode channels. *Int J Hydrogen Energy* 2006;31(8):1031–9.
- [22] Alizadeh E, et al. Numerical and experimental investigation of cascade type serpentine flow field of reactant gases for improving performance of PEM fuel cell. *Int J Hydrogen Energy* 2017;42(21):14708–24.
- [23] Wilberforce T, et al. Modelling and simulation of Proton Exchange Membrane fuel cell with serpentine bipolar plate using MATLAB. *Int J Hydrogen Energy* 2017;42(40):25639–62.
- [24] Li S, Sundén B. Effects of gas diffusion layer deformation on the transport phenomena and performance of PEM fuel cells with interdigitated flow fields. *Int J Hydrogen Energy* 2018;43(33):16279–92.
- [25] Chen S, Zhang X, Liu H. Effect of pressure difference between adjacent channels in an adjustable flow field in PEM fuel cells. *Int J Hydrogen Energy* 2017;42(7):4667–72.
- [26] Park J, Li X. An experimental and numerical investigation on the cross flow through gas diffusion layer in a PEM fuel cell with a serpentine flow channel. *J Power Sources* 2007;163(2):853–63.
- [27] Hsieh S-S, Her B-S, Huang Y-J. Effect of pressure drop in different flow fields on water accumulation and current distribution for a micro PEM fuel cell. *Energy Convers Manag* 2011;52(2):975–82.
- [28] Hsieh S-S, Huang Y-J, Her B-S. Pressure drop on water accumulation distribution for a micro PEM fuel cell with different flow field plates. *Int J Heat Mass Tran* 2009;52(23):5657–9.
- [29] Wood DL, Yi JS, Nguyen TV. Effect of direct liquid water injection and interdigitated flow field on the performance of proton exchange membrane fuel cells. *Electrochim Acta* 1998;43(24):3795–809.
- [30] Owejan JP, et al. In situ investigation of water transport in an operating PEM fuel cell using neutron radiography: Part 2 – transient water accumulation in an interdigitated cathode flow field. *Int J Heat Mass Tran* 2006;49(25):4721–31.
- [31] Spornjak D, Prasad AK, Advani SG. In situ comparison of water content and dynamics in parallel, single-serpentine, and interdigitated flow fields of polymer electrolyte membrane fuel cells. *J Power Sources* 2010;195(11):3553–68.
- [32] Belhadj M, et al. Current density distributions in polymer electrolyte fuel cells: a tool for characterisation of gas distribution in the cell and its state of health. *Chem Eng Sci* 2018;185:18–25.
- [33] Iranzo A, et al. Water build-up and evolution during the start-up of a PEMFC: visualization by means of Neutron Imaging. *Int J Hydrogen Energy* 2017;42(19):13839–49.
- [34] Liu X, et al. Flow dynamic characteristics in flow field of proton exchange membrane fuel cells. *Int J Hydrogen Energy* 2008;33(3):1040–51.
- [35] Litster S, et al. Active water management for PEM fuel cells. *J Electrochem Soc* 2007;154(10):B1049–58.
- [36] Konno N, et al. Development of Compact and high-performance fuel cell stack. *SAE Int. J. Alt. Power* 2015;4(1):123–9.
- [37] Nonobe Y. Development of the fuel cell vehicle mirai. *IEEJ Trans Electr Electron Eng* 2017;12(1):5–9.
- [38] Yoshida T, Kojima K. Toyota MIRAI fuel cell vehicle and progress toward a future hydrogen society. *The Electrochemical Society Interface* 2015;24(2):45–9.
- [39] Metz T, et al. Passive water removal in fuel cells by capillary droplet actuation. *Sensor Actuator Phys* 2008;143(1):49–57.
- [40] Koresawa R, Utaka Y. Water control by employing microgrooves inside gas channel for performance improvement in polymer electrolyte fuel cells. *Int J Hydrogen Energy* 2015;40(25):8172–81.
- [41] Ge S-H, Li X-G, Hsing I-M. Water management in PEMFCs using absorbent wicks. *J Electrochem Soc* 2004;151(9):B523–8.
- [42] Ge S, Li X, Hsing IM. Internally humidified polymer electrolyte fuel cells using water absorbing sponge. *Electrochim Acta* 2005;50(9):1909–16.
- [43] Strickland DG, Santiago JG. In situ polymerized wicks for passive water management and humidification of dry gases. *Meet Abstr* 2009;(10):819. MA2009-02.
- [44] Strickland DG, Santiago JG. In situ-polymerized wicks for passive water management in proton exchange membrane fuel cells. *J Power Sources* 2010;195(6):1667–75.

- [45] Yi JS, Yang JD, King C. Water management along the flow channels of PEM fuel cells. *AIChE J* 2004;50(10):2594–603.
- [46] Wang Z, et al. Improvement of PEMFC water management by employing water transport plate as bipolar plate. *Int J Hydrogen Energy* 2017;42(34):21922–9.
- [47] Weber AZ, Darling RM. Understanding porous water-transport plates in polymer-electrolyte fuel cells. *J Power Sources* 2007;168(1):191–9.
- [48] Fabian T, et al. Active water management at the cathode of a planar air-breathing polymer electrolyte membrane fuel cell using an electroosmotic pump. *J Power Sources* 2010;195(11):3640–4.
- [49] Brett DJL, Brandon NP. Review of materials and characterization methods for polymer electrolyte fuel cell flow-field plates. *J Fuel Cell Sci Technol* 2006;4(1):29–44.
- [50] Haase S, et al. Current density and catalyst-coated membrane resistance distribution of hydro-formed metallic bipolar plate fuel cell short stack with 250 cm² active area. *J Power Sources* 2016;301:251–60.
- [51] Jung S-P, et al. Development of novel proton exchange membrane fuel cells using stamped metallic bipolar plates. *J Power Sources* 2015;283:429–42.
- [52] Meyer Q, et al. Combined current and temperature mapping in an air-cooled, open-cathode polymer electrolyte fuel cell under steady-state and dynamic conditions. *J Power Sources* 2015;297:315–22.
- [53] Meyer Q, et al. System-level electro-thermal optimisation of air-cooled open-cathode polymer electrolyte fuel cells: air blower parasitic load and schemes for dynamic operation. *Int J Hydrogen Energy* 2015;40(46):16760–6.
- [54] Brett DJL, et al. Measurement of the current distribution along a single flow channel of a solid polymer fuel cell. *Electrochem Commun* 2001;3(11):628–32.
- [55] Knowles MRH, et al. Micro-machining of metals, ceramics and polymers using nanosecond lasers. *Int J Adv Manuf Technol* 2007;33(1):95–102.
- [56] Gruner A, Schille J, Loeschner U. Experimental study on micro hole drilling using ultrashort pulse laser radiation. *Physics Procedia* 2016;83:157–66.
- [57] Ghoreishi M, Low DKY, Li L. Comparative statistical analysis of hole taper and circularity in laser percussion drilling. *Int J Mach Tool Manufact* 2002;42(9):985–95.
- [58] Bonn D, et al. Wetting and spreading. *Rev Mod Phys* 2009;81(2):739–805.
- [59] Meyer Q, et al. Investigation of hot pressed polymer electrolyte fuel cell assemblies via X-ray computed tomography. *Electrochim Acta* 2017;242:125–36.
- [60] Bachman J, et al. Investigation of polymer electrolyte membrane fuel cell parallel flow field with induced cross flow. *J Power Sources* 2012;198:143–8.
- [61] Siefert NS, Litster S. Voltage loss and fluctuation in proton exchange membrane fuel cells: the role of cathode channel plurality and air stoichiometric ratio. *J Power Sources* 2011;196(4):1948–54.
- [62] Deevanhxay P, et al. Effect of liquid water distribution in gas diffusion media with and without microporous layer on PEM fuel cell performance. *Electrochem Commun* 2013;34:239–41.
- [63] Deevanhxay P, et al. Investigation of water accumulation and discharge behaviors with variation of current density in PEMFC by high-resolution soft X-ray radiography. *Int J Hydrogen Energy* 2011;36(17):10901–7.
- [64] Mason TJ, et al. A study of the effect of water management and electrode flooding on the dimensional change of polymer electrolyte fuel cells. *J Power Sources* 2013;242:70–7.
- [65] Prasad KBS, Jayanti S. Effect of channel-to-channel cross-flow on local flooding in serpentine flow-fields. *J Power Sources* 2008;180(1):227–31.
- [66] Zhang J, et al. PEM fuel cell relative humidity (RH) and its effect on performance at high temperatures. *Electrochim Acta* 2008;53(16):5315–21.
- [67] Novitski D, Holdcroft S. Determination of O₂ mass transport at the Pt | PFSA ionomer interface under reduced relative humidity. *ACS Appl Mater Interfaces* 2015;7(49):27314–23.
- [68] Neyerlin KC, et al. Effect of relative humidity on oxygen reduction kinetics in a PEMFC. *J Electrochem Soc* 2005;152(6):A1073–80.
- [69] Fabian T, et al. The role of ambient conditions on the performance of a planar, air-breathing hydrogen PEM fuel cell. *J Power Sources* 2006;161(1):168–82.
- [70] Raileanu Ilie VA, Martemianov S, Thomas A. Investigation of the local temperature and overheat inside the membrane electrode assembly of PEM fuel cell. *Int J Hydrogen Energy* 2016;41(34):15528–37.
- [71] Meyer Q, et al. Optimisation of air cooled, open-cathode fuel cells: current of lowest resistance and electro-thermal performance mapping. *J Power Sources* 2015;291:261–9.
- [72] Trabold TA, et al. In situ investigation of water transport in an operating PEM fuel cell using neutron radiography: Part 1 – experimental method and serpentine flow field results. *Int J Heat Mass Tran* 2006;49(25):4712–20.
- [73] Cao T-F, et al. Numerical investigation of the coupled water and thermal management in PEM fuel cell. *Appl Energy* 2013;112:1115–25.
- [74] Cao T-F, et al. Modeling the temperature distribution and performance of a PEM fuel cell with thermal contact resistance. *Int J Heat Mass Tran* 2015;87:544–56.
- [75] Sasmito AP, Kurnia JC, Mujumdar AS. Numerical evaluation of various gas and coolant channel designs for high performance liquid-cooled proton exchange membrane fuel cell stacks. *Energy* 2012;44(1):278–91.
- [76] Hickner MA, et al. Real-time imaging of liquid water in an operating proton exchange membrane fuel cell. *J Electrochem Soc* 2006;153(5):A902–8.
- [77] Xue D, Dong Z. Optimal fuel cell system design considering functional performance and production costs. *J Power Sources* 1998;76(1):69–80.
- [78] Gemmen RS, Johnson CD. Evaluation of fuel cell system efficiency and degradation at development and during commercialization. *J Power Sources* 2006;159(1):646–55.